POLITECNICO DI TORINO
Repository ISTITUZIONALE

Ammonia-based direct reduction of iron ores: Modelling and experimental assessment

Original
Ammonia-based direct reduction of iron ores: Modelling and experimental assessment / Paziente, A., Magnino, A., Gandiglio, M., Mastropasqua, L.. - In: CHEMICAL ENGINEERING JOURNAL. - ISSN 1385-8947. - 545:(2026). [10.1016/j.cej.2026.178542]

Availability:
This version is available at: 11583/3013510 since: 2026-07-24T09:29:28Z

Publisher:
Elsevier

Published
DOI:10.1016/j.cej.2026.178542

Terms of use:

This article is made available under terms and conditions as specified in the corresponding bibliographic description in the repository

Publisher copyright

(Article begins on next page)

23 October 2026

Chemical Engineering Journal 545 (2026) 178542

Contents lists available at ScienceDirect

Chemical Engineering Journal

journal homepage: www.elsevier.com/locate/cej

Ammonia-based direct reduction of iron ores: Modelling and experimental assessment

Angelo Paziente [a], Alessandro Magnino [a], Marta Gandiglio [a,*], Luca Mastropasqua [b]

[a] Department of Energy, Politecnico di Torino, Corso Duca degli Abruzzi 24, 10129, Torino, Italy
[b] Department of Mechanical Engineering, University of Wisconsin-Madison, Engineering Research Building 1500 Engineering Drive, Madison, WI, 53706, United States of America

ARTICLE INFO

Keywords:
Steel industry
Direct reduction of Iron
Ammonia
Ammonia-based direct reduction
Unreacted shrinking Core model

ABSTRACT

The iron and steel industry is a cornerstone of the EU economy, producing materials essential to various industrial sectors but contributing approximately 5% of the EU's total CO_2 emissions. Among the most promising pathways for decarbonising the steel industry is the adoption of Direct Reduced Iron (DRI) technology, particularly hydrogen-based DRI (H_2-DRI), which has the potential to eliminate CO_2 emissions during the most carbon-intensive stage of steel production by using hydrogen as a reducing agent instead of fossil fuels. However, hydrogen's low volumetric energy density and the complexity of its transport and storage present practical limitations to large-scale deployment. In this context, ammonia emerges as a compelling alternative energy carrier, thanks to its higher volumetric density, established logistics infrastructure, and the ability to decouple hydrogen production from its point of use.

This work investigates the feasibility of ammonia-driven DRI (A-DRI) by combining thermodynamic analysis, kinetic modelling, and experimental characterisation of porosity and phase evolution during hydrogen reduction. A reactor-scale model based on the Unreacted Shrinking Core (USC) framework is developed to quantify the coupled effects of temperature, gas composition, and mass-transfer resistances, while ex-situ measurements establish correlations between metallisation, pore structure, and diffusion behaviour.

Results show that ammonia can be integrated into a shaft furnace without altering the fundamental reduction pathway: in-furnace cracking on metallic iron efficiently releases hydrogen, whereas ammonia itself does not participate directly in iron-oxide reduction. Although its use increases the thermal load, appropriate gas-recirculation strategies enable operating conditions compatible with existing H_2-DRI designs. Overall, A-DRI may provide a promising route to low-carbon ironmaking while mitigating the infrastructural barriers associated with large-volume hydrogen supply.

1. Introduction

In recent decades, global steel demand has risen sharply to support the socio-economic development of both industrialized and emerging countries. Steel is essential to the energy sector, used in wind turbines, nuclear vessels, dams, electric vehicles, and power infrastructure, highlighting its importance in the transition to cleaner energy. Global steel production has more than doubled in the past 20 years [1]. However, the industry contributes to 7–9% of global CO_2 emissions and about to 5% of Europe's total emissions [2].

Currently, steel is produced through three main process routes, each characterized by different energy demands and carbon intensities. The blast furnace-basic oxygen furnace (BF-BOF) route remains the dominant pathway, accounting for approximately 72% of global crude steel output. Electric arc furnaces (EAF) using scrap steel contributes to about 21%, while the direct reduction-electric arc furnace (DRI-EAF) route represents the remaining 7% of worldwide production [3]. Among the different steel production routes, the BF-BOF pathway is by far the most carbon-intensive, as it relies on coke and coal as reducing agents. The average direct CO_2 emissions are approximately 2.2–2.3 t_{CO2} per tonne of crude steel for the BF-BOF route, compared to 0.3–0.5 t_{CO2}/t for the EAF route, depending on the carbon intensity of the electricity mix [4].

Although increasing steel scrap recycling offers clear environmental benefits, its potential is constrained by scrap availability and quality

* Corresponding author.
E-mail address: marta.gandiglio@polito.it (M. Gandiglio).

https://doi.org/10.1016/j.cej.2026.178542
Received 12 March 2026; Received in revised form 4 June 2026; Accepted 17 June 2026
Available online 18 June 2026
1385-8947/© 2026 The Author(s). Published by Elsevier B.V. This is an open access article under the CC BY-NC-ND license (http://creativecommons.org/licenses/by-nc-nd/4.0/).

limitations, meaning that demand for primary steel will persist in the coming decades [5]. Additionally, nearly half of today's BF capacity will require major reinvestment by 2030 [2], raising concerns about locking in carbon emissions for the long term or making investments that may later become obsolete [6].

A promising alternative to conventional BF ironmaking is direct reduced iron (DRI) technology, in which iron ore is reduced using a gas mixture of hydrogen and carbon monoxide, derived from natural gas reforming [7]. The resulting sponge iron is then melted in an EAF, yielding steel with an average carbon intensity of about 1.4 t_{CO2} per tonne of crude steel for natural-gas-based DRI-EAF routes [4].

The integration of hydrogen-based direct reduced of iron (H_2-DRI) with EAF steelmaking has recently emerged as a viable pathway to drastically reduce CO_2 emissions. In this configuration, hydrogen reacts with iron ore to produce metallic iron and water vapour as a byproduct, enabling up to 90–95% reduction in direct CO_2 emissions compared to natural gas-based DRI [8]. However, the extent of decarbonization strongly depends on the hydrogen production route. Only hydrogen derived via electrolysis powered by renewable energy sources (RES) ensures minimal upstream CO_2 emissions, yet most hydrogen today is produced from fossil fuels through steam methane reforming, while renewable hydrogen accounts for only about 3% of global production [9]. Moreover, the intermittent nature of RES conflicts with the continuous operation required by shaft furnaces, necessitating large-scale hydrogen storage systems to maintain process reliability [10]. Finally, when onsite hydrogen production is unfeasible or uneconomical, a dedicated hydrogen transport infrastructure becomes necessary.

In this context, ammonia emerges as a compelling alternative energy carrier. Due to its higher volumetric density and long-standing industrial use, ammonia offers several practical advantages [11]. It can be employed directly as fuel or thermochemically dissociated to release hydrogen. The viability of ammonia as a hydrogen carrier, however, critically depends on the availability of a safe and scalable transport infrastructure. Currently, approximately 170 ships worldwide are capable of carrying ammonia, with around 40 vessels dedicated exclusively to its transport, suggesting a growing logistical base for large-scale deployment [12]. Nonetheless, among the stages involved in ammonia-based hydrogen transport, the cracking step remains the most energy-intensive and least efficient, due to the high temperature required and the incomplete conversion typically achieved [11].

Integrating ammonia directly into a DRI shaft furnace (ammonia-based direct reduced iron, A-DRI) offers a novel and promising alternative. At high temperatures characteristic of DRI operation, metallic iron promotes the in-situ cracking of ammonia, thereby releasing hydrogen directly within the furnace. This eliminates the need for an external endothermic cracking and avoids the associated heat input. Under typical furnace inlet conditions, ammonia first contacts pure iron on the pellet surfaces, maximizing cracking efficiency. The hydrogen produced then drives the sequential reduction of iron oxides along the furnace height. However, the higher endothermicity of ammonia decomposition compared with pure hydrogen reduction introduces more stringent thermal management constraints, potentially requiring higher gas inlet temperatures or increased reducing-gas flow rates.

A detailed understanding of the thermodynamics and reaction mechanisms governing ammonia decomposition, as well as its interaction with iron oxide pellets under DRI conditions, is therefore essential to assess the feasibility of NH_3-based steelmaking routes. The following sections examine these aspects in detail, with specific attention to equilibrium behaviour, reduction kinetics, and the catalytic role of metallic iron.

1.1. Kinetics and reaction pathways of Iron oxide reduction by hydrogen

The transition to hydrogen-based iron ore reduction places renewed attention on the microstructural evolution of iron ore pellets. Although the thermodynamic pathway from hematite to metallic iron is well established, the overall reduction behaviour is strongly governed by kinetic factors and by the morphological transformations that occur within the pellets during reaction. Temperature, gas-solid mass transfer, porosity development, sintering phenomena, and phase transformation mechanisms collectively shape the internal structure of the pellet as reduction progresses. These coupled effects not only determine the reaction rate but also lead to macroscopic dimensional changes, such as swelling or densification, that can affect reactor performance and process stability.

The time evolution of the reduction rate of an iron-oxide pellet under hydrogen flow reflects the coupling of transport and microstructural phenomena acting across multiple length scales, as schematically illustrated in Fig. 1. At the pellet scale, reduction progresses through a moving reaction front: as an external product layer forms, hydrogen must diffuse through the increasingly thick, porous shell to reach the inner oxide, while the generated steam counter-diffuses outward. This additional transport resistance becomes progressively more relevant as reduction proceeds and a metallic iron layer develops at the pellet surface [13].

At the same time, the reduction pathway is stepwise, following the sequence hematite (Fe_2O_3) → magnetite (Fe_3O_4) → wüstite (FeO) → metallic iron (Fe). The appearance of intermediate phases and the persistence of partially reduced regions imply that different local morphologies and transport properties can coexist within the same pellet during transient operation. As oxygen is removed from the oxide lattice, the pore network evolves, generally promoting pore growth and coalescence and thus facilitating gas transport. However, this trend competes with thermally activated sintering, which promotes densification through grain coarsening and pore shrinkage, thereby reducing permeability and slowing down intra-pellet mass transport.

Finally, at the micro-scale, the overall rate is controlled by surface processes such as adsorption and dissociation of hydrogen, formation and desorption of water, and vacancy generation at the solid surface. The interplay between these elementary steps, the evolving pore network, and the diffusion of gaseous species through the product layer determines the observed reduction kinetics along the furnace.

The reduction proceeds step-wisely with FeO appearance only after complete transformation of Fe_2O_3, and metallic iron (Fe) presence even when some Fe_3O_4 is still present [14,15]. During reduction, pellet porosity generally increases due to the removal of oxygen from the oxide lattice [14], which enhances gas diffusion and accelerates reaction rates. However, this porosity evolution is complex to predict because sintering acts concurrently in the opposite direction, promoting densification of the material.

Sintering is a time-dependent, thermally activated process that strongly affects both the microstructure and the kinetics of hydrogen reduction. Extended exposure to high temperatures causes grain coarsening and pore shrinkage, leading to overall pellet densification. The process is further complicated by the sequence of phase transformations (hematite → magnetite → wüstite → iron), each characterized by different sintering activation temperatures and thermal expansion behaviours [16].

Magnetite and hematite exhibit different sintering behaviours: magnetite starts to sinter at lower temperatures, typically in the range 900–1100 °C, whereas hematite sintering becomes significant at higher temperatures, approximately between 1100 and 1350 °C [17].

The volumetric evolution of iron ore pellets during reduction is commonly expressed through the Reduction Swelling Index (RSI), which quantifies the relative change in pellet volume, normalised by its initial volume, thus capturing both swelling and densification phenomena. Several studies agree on the positive effect of temperature on the rate of reaction [15,18,19] a behaviour linked both to thermodynamics and kinetics.

He et al. [20] performed experiments between 600 °C and 1050 °C with 50 °C steps to examine the sintering behaviour of metallic iron. Sintering began above 750 °C, with porosity decreasing from 61% at

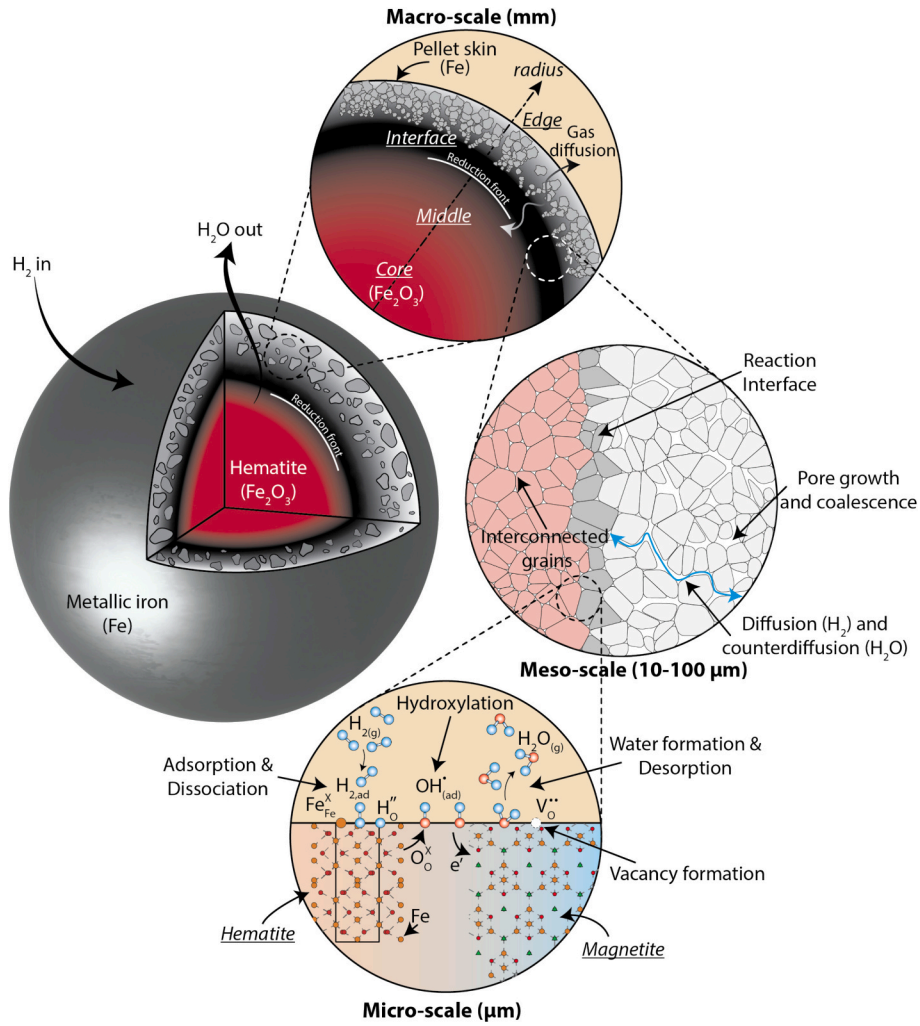

Fig. 1. Multiscale schematic of iron-oxide reduction under hydrogen flow, illustrating the coupled phenomena occurring at pellet (macro), pore-network (*meso*), and surface-reaction (micro) scales.

600 °C to 49% at 1050 °C. From 750 °C to 950 °C, no reaction slowdown was observed due to temperature-enhanced surface reactions and gas diffusion. A reduction in the reaction rate occurred above 950 °C, linked to the phase transition from α-Fe to γ-Fe at 910 °C, causing densification and slowing the reduction process.

Temperature and reducing gas composition affect pellet porosity during reduction, revealing increased pore and grain size with temperature due to densification and iron layer interconnection [21]. Volume measurements through displacements showed an initial volume increase due to the anisotropic transformation of Fe_2O_3 to Fe_3O_4, peaking at around 40% reduction, followed by an RSI drop attributed to sintering and recrystallization of metallic iron [21]. Yi et al. [22] performed X-ray Diffraction (XRD) analysis on samples showing maximum RSI peaks to understand the expansion of reduced iron ore. The results indicated that wüstite was the dominant phase, with smaller amounts of iron and magnetite present. Pellets reduced at higher temperatures showed greater RSI due to increased wüstite. As hematite reduced to magnetite, wüstite formed, causing significant volume expansion. Later, as wüstite was replaced by metallic iron, the compacts shrank due to sintering and densification.

1.2. Thermochemical decomposition of ammonia and its interaction with Iron oxides

In ammonia-based direct reduction (A-DRI), introducing ammonia as a hydrogen carrier requires understanding not only its thermodynamic behaviour but also the kinetic limitations associated with its high-temperature decomposition. When ammonia enters a DRI shaft furnace, its catalytic conversion to hydrogen is heavily mediated by the freshly reduced metallic iron surface. The reaction mechanism proceeds via the transport of NH_3 to the iron crystallites surface, followed by sequential dissociative adsorption to form atomic N and H species. [22] While hydrogen atoms rapidly desorb as molecular H_2, the accumulated nitrogen atoms either recombine and desorb as N_2 gas or diffuse into the iron matrix to form nitrides [23], particularly at elevated ammonia partial pressures [24], according to the reaction:

$$2xFe + 2NH_3 \leftrightarrows 2Fe_xN + 3H_2 \quad (1)$$

It is therefore useful to distinguish between two coupled but distinct phenomena: ammonia catalytic decomposition, which supplies hydrogen for iron oxide reduction, and iron nitridation, which may occur only under specific temperature and gas-composition conditions when the local nitriding potential is sufficiently high.

Kinetic studies of ammonia decomposition over iron catalysts showed that the reaction rate increases with temperature and it is promoted by higher hydrogen pressure [25]. At 1200 K, the reaction follows first-order kinetics with respect to ammonia concentration due to fast nitrogen desorption. At lower temperatures or high ammonia concentrations, the reaction order shifts to zero because of higher surface saturation with nitrogen adsorbed nitrogen. The concentration

threshold at which the transition from first- to zero-order kinetics occurs increases as temperature rises.

Recent work by Mittal and Davis [26] demonstrated that ammonia can act as a highly effective reducing agent for iron oxides. Under high-temperature (at 1000 °C) and high-flow conditions, the authors showed that NH_3 decomposes nearly instantaneously to form a H_2-N_2 mixtures, achieving complete reduction of iron oxide in only 1 min, with ammonia utilization up to 64%. Hosokai et al. [27], in 2010, had already demonstrated the reduction of hematite with ammonia at various temperatures, showing that direct ammonia reduction ($Fe_2O_3 + 2NH_3 \rightarrow 2Fe + N_2 + 3H_2O$) only occurs <430 °C, while an indirect reduction mechanism (NH_3 cracking + H_2 reduction) is favoured at temperatures >530 °C. The catalytic role of metallic iron is further supported by Ma et al. [23], who reported that the porous iron matrix formed during ammonia-based reduction can promote NH_3 decomposition autocatalytically, thereby generating hydrogen close to the reacting solid surface. In the present reactor-scale model, this effect is represented in a simplified one-dimensional form by activating finite-rate ammonia cracking in the metallic-iron-rich region of the shaft furnace.

The phase boundary between body-centred cubic metallic iron ($\alpha - Fe$) and various iron nitride phases ($\gamma' - Fe_4 - N$ and $\varepsilon - Fe_{3-x} - N$) is governed by the nitriding potential (P_N), which is a technical measure of the surface nitrogen activity [23].

$$P_N = \frac{P_{N,\ NH_3}}{P_{N,H_2}^{3/2}} \tag{2}$$

A recent review by Triana et al. [19] provided a comprehensive thermodynamic analysis of the reactions involved in the reduction of iron oxides with ammonia, evaluating ammonia decomposition behaviour, the stability of intermediate and nitride phases, and the equilibrium conditions governing ammonia-based direct reduction.

As nitridation proceeds, the ammonia decomposition reaction rate decreases until gas-solid equilibrium is reached, beyond which the system stabilizes. Studies using NH_3-H_2 mixtures with ammonia ranging from 0 to 100%, found a linear correlation between the decomposition rate and the logarithm of the nitriding potential [28]. Experimental evidence shows that iron nitrides are unstable phases at or above 700 °C [25,29], indicating that the critical nitriding potential required for their stability increases with temperature and strongly depends on the NH_3/H_2 ratio.

Temperature-programmed reduction (TPR) combined with in-situ X-ray diffraction (XRD) analyses under 100% ammonia on hematite powder showed that ammonia first reduces hematite to magnetite at approximately 500 °C, while metallic iron formation occurs at around 600 °C through hydrogen generated by ammonia decomposition [30]. The resulting metallic iron can then be nitrided by residual ammonia. In-situ XRD further revealed that nitridation starts at approximately 350 °C and leads to the formation of ε-$Fe_{3-x}N$ above 550 °C, whereas nitride phases decompose into α-Fe and nitrogen gas above approximately 650 °C [30]. Higher nitriding potential was found to increase the nitrogen content in the sample and decrease ammonia conversion, consistently with previous observations on ammonia decomposition over iron catalysts [28]. Ma et al. [23] detected no NOx production and formation of Fe_4N, localized mainly on the surface. This nitride layer may provide temporary protection against oxidation during transport and is fully removed during melting in the EAF.

1.3. Aim and novelty of the study

Despite the growing interest in ammonia as an alternative hydrogen carrier for hydrogen-based direct reduction, the existing literature remains limited. Previous studies have demonstrated that iron oxides can be successfully reduced using ammonia at high temperatures, and some experimental studies have explored the kinetics and product evolution during reduction. However, to date, no comprehensive process-level analysis has coupled thermodynamic feasibility, reactor-scale kinetic modelling, and experimentally derived transport properties specifically tailored to ammonia-based DRI. In particular, no study has yet quantified the flow rates, recirculation requirements, or temperature constraints necessary to operate a fully ammonia-fuelled shaft furnace under industrially relevant conditions.

The aim of this work is therefore to assess the feasibility of ammonia-driven direct reduction of iron (A-DRI) by integrating:

- a thermodynamic assessment of both the reducing zone and cooling zones of a DRI shaft furnace, to determine inlet temperatures and mass flow rates of ammonia and recirculated gases;
- a kinetic reactor model based on a Plug Flow Reactor (PFR) coupled with the Unreacted Shrinking Core (USC) model, to describe gas-solid reduction within the furnace.

A key modelling challenge concerns the description of diffusion resistance inside iron oxide pellets, which evolves significantly during reduction. To address this, dedicated experimental work is conducted to quantify the variation of porosity with metallisation. Using densitometry and SEM-XRD characterisation, the contributions of pore volume and skeletal volume are separately measured, enabling empirical extraction of effective diffusion coefficients for hematite, magnetite, wüstite, and metallic iron. These experimentally derived parameters were incorporated into the shaft-furnace kinetic model for the first time.

The novelty of this study lies in delivering the first combined thermal and kinetic evaluation of direct ammonia injection into a DRI shaft furnace. Whereas previous works primarily assessed the fundamental feasibility of ammonia as a reducing agent, the present analysis quantifies how ammonia affects furnace behaviour and operating conditions. Specifically, the model determines the maximum ammonia feed rates that can be supplied without compromising temperature, reaction progression, or metallisation performance, as well as the associated requirements for hydrogen-nitrogen recirculation flows needed to sustain continuous industrial-scale operation. Furthermore, the experimentally supported description of reduction-induced microstructural evolution provides a more accurate representation of intra-pellet mass-transfer resistance, establishing a modelling approach that can be directly applied to future A-DRI process design.

To support this analysis, Section 2 presents the thermodynamic framework, the experimental methodology for porosity characterisation, and the formulation of the kinetic shaft-furnace model. Section 3 discusses the resulting thermodynamic balances, experimental findings, and kinetic simulations, highlighting their implications for ammonia-based DRI operation. Finally, Section 4 summarizes the main conclusions of the study and outlines directions for future research.

2. Materials and methods

Section 2 is structured into three parts. Section 2.1 presents the thermodynamic framework used to determine the ammonia and gas-flow requirements for the A-DRI process. Section 2.2 describes the experimental methodology adopted to quantify porosity evolution and extract phase-specific transport parameters. These experimentally derived parameters are then used in Section 2.3, where the kinetic shaft-furnace model is formulated through a Plug Flow Reactor (PFR) representation coupled with the Unreacted Shrinking Core (USC) approach.

2.1. Thermodynamic model

A thermodynamic analysis is conducted to quantify the gas requirements associated with the reduction of iron oxides in the shaft furnace, considering both the cooling and the reducing zones. The analysis begins with the cooling section, since the gas exiting this zone becomes the inlet to the reducing zone and thus determines the thermal and chemical boundary conditions of the overall process.

In the proposed A-DRI configuration, ammonia is selected as the cooling gas and it is injected from the bottom of the cooling zone, where it flows counter-current to the descending metallic iron pellets. During this interaction, ammonia absorbs sensible heat from the pellets, promoting their cooling while simultaneously undergoing thermal cracking.

In conventional hydrogen-based shaft furnaces, the cooling gas typically consists of a hydrocarbon stream used to carburize and protect the pellets from re-oxidation. In contrast, in the A-DRI concept, ammonia acts as an active medium capable of decomposing at high temperature into hydrogen and nitrogen, thereby supplying both reducing and carrier gases for the upper part of the shaft. Depending on the local temperature and NH_3/H_2 ratio, transient iron nitride formation may occur on metallic iron surfaces; however, persistent nitridation is not included in the present thermodynamic model and is discussed as a limitation of the kinetic analysis.

Mass and energy balances are applied to the cooling zone control volume to determine the maximum amount of ammonia that can be decomposed while keeping the furnace thermally self-sustained. In this region, the descending hot pellets provide the sensible heat that is transferred to the injected ammonia stream, simultaneously cooling the solid bed and supplying the endothermic heat required for ammonia preheating and cracking into hydrogen and nitrogen. Once the outlet conditions of the cooling zone are determined, the reducing zone is evaluated using the same thermodynamic framework. Here, the endothermic reduction of hematite and the heat required for ammonia decomposition result in a substantial thermal demand. For this reason, the inlet gas to the reducing zone consists of fresh ammonia, sized to supply the exact stoichiometric hydrogen demand, and a fraction of hot recirculated gas, which provides the necessary sensible heat [31].

All assumptions and governing balance equations used for both zones are summarised in Table 1.

Table 1
Summary of thermodynamic assumptions and governing equations for the cooling and reducing zones, including inlet/outlet conditions and energy balance formulations.

Assumptions	Cooling zone	Reducing zone
Pellets mass, temperature and composition	Inlet: 1000 kg of pure Fe at 1200 °C Outlet: 1000 kg of pure Fe at 50°C	Inlet: 1430 kg of 100% Fe_2O_3 at 50 °C Outlet: 1000 kg of pure Fe at 1250 °C
Cooling gas mass, temperature and composition	Inlet: unknown kg of 100% NH_3 at 25 °C Outlet: unknown kg of N_2 and H_2 at 1200 °C	n.a.
Reducing gas	n.a.	Inlet: NH_3 (stoichiometric amount to supply the hydrogen required for hematite reduction) at 1250 °C; − H_2-N_2 mixture from the cooling zone at 1200 °C; Recirculated gas (75% H_2, 25% N_2) at 1250 °C Outlet: H_2, N_2, and H_2O at 400 °C
Reactions modelled	Ammonia cracking: $2NH_3 \rightarrow N_2 + 3H_2$	Ammonia cracking and hydrogen−based reduction: $Fe_2O_3 + 3H_2 \rightarrow 2Fe + 3H_2O$
Reaction enthalpies [J/mol]	$\Delta H_{r,crk}(T) = 3 \cdot \Delta H_{H_2}(T) + \Delta H_{N_2}(T) - 2 \cdot \Delta H_{NH_3}(T)$	$\Delta_r H_{red}(T) = 3 \cdot \Delta H_{H_2O}(T) + 2 \cdot \Delta H_{Fe}(T) - 3 \cdot \Delta H_{H_2}(T) - \Delta H_{Fe_2O_3}(T)$
Energy balance contribution	Sensible heat of hot metallic iron pellets; Sensible heat of inlet NH_3; Endothermic heat of ammonia cracking	Sensible heat of hematite pellets; Sensible heat of inlet and recirculated gases; Endothermic heats of iron oxide reduction and ammonia cracking
Energy balance formulation	Steady-state energy balance equating inlet sensible heats to outlet sensible heats and reaction enthalpy	Steady-state energy balance including recirculated gas contribution to satisfy the thermal demand of reduction and cracking
Thermochemical parameters derived from NIST database as a function of temperature	Temperature-dependent enthalpies and heat capacities derived from the NIST database	
Additional assumptions	$\Delta H_{r,crk}(T)$, evaluated at 600 °C; Complete NH_3 conversion assumed only for preliminary thermodynamic sizing. Persistent nitridation neglected in the thermodynamic balance.	$\Delta H_{r,crk}(T)$ evaluated at 1100 °C; $\Delta_r H_{red}(T)$ evaluated at 800 °C; Complete NH_3 conversion used only in the global thermodynamic balance; finite-rate cracking is treated in the kinetic model.

2.2. Experimental setup

Hematite pellets (4 g) were prepared using ≥96% Iron (III) oxide powder (<5 μm, Sigma-Aldrich) and a YLJ-CIP-20B Cold Isostatic Press (30 mm ID, 300 MPa max, MTI Group). The experimental campaign was designed to quantify both global and local porosity evolution during hydrogen reduction, and to extract phase-specific transport parameters for model integration. The powder was pressed at 83 MPa for 5 min using a manual oil pump to apply 6 t of force, ensuring sufficient mechanical strength. After a sintering cycle (heating rate 5 °C/min from room temperature up to 800 °C for 3 h), the hematite pellets were then reduced at 800 °C in a three-zone 80 mm OD Tube Furnace (Across International) under a flow of 25% hydrogen in argon at 250 SCCM (standard cubic centimeters per minute). Reduction tests were performed at multiple residence times (0, 2.5, 5, 10, 15, 30, 60, 75, 120, 150, and 180 min) to obtain a wide range of metallisation degrees; two pellets were produced for each condition. Fig. 2 illustrates the overall experimental workflow for porosity determination. After reduction, each pellet was subjected to density measurement using a Sartorius YDK03 density determination kit, enabling the calculation of the geometric volume of the pellet as the sum of the skeletal volume and pore volume. The porosity values were then plotted against the metallisation degree and fitted with a polynomial trendline incorporated into the kinetic model. The porosity obtained from density measurements represents the global porosity of the pellet, i.e., the volume fraction of voids averaged over the entire sample. However, the kinetic model requires a local porosity profile, which depends both on the iron oxide phase present (hematite, magnetite, wüstite, or metallic iron) and on the radial position within the pellet. Local variations arise because the reduction front progresses from the exterior toward the core, producing distinct microstructures and pore networks as each oxide transforms into the next. SEM and XRD analyses were therefore performed at multiple radial locations and correlated with the iron-oxide distribution. Specifically, two representative pellets - reduced for 5 and 60 min - were selected for SEM and XRD analyses, as they capture both an early-stage and an advanced-stage reduction regime. They were embedded in conductive epoxy resin (ConductoBed, SPI Supplies; 2:1 resin-to-hardener ratio), cured at 70 °C for 24 h, and sectioned using an electric saw to obtain precise cross-sections for microstructural and phase characterisation. SEM imaging (Zeiss Gemini 300) was carried out at multiple radial positions, and porosity was quantified using ImageJ. XRD measurements (Bruker D8 diffractometer) were performed at four radial positions - edge, interface, middle, and core - to identify the oxide phases present and track the advancement of the reduction front.

To integrate the experimental findings into the kinetic model, the porosity values measured with the densitometer were used as a baseline to assign specific porosity levels to the different iron oxide phases: magnetite, wüstite, and metallic iron. These values were derived

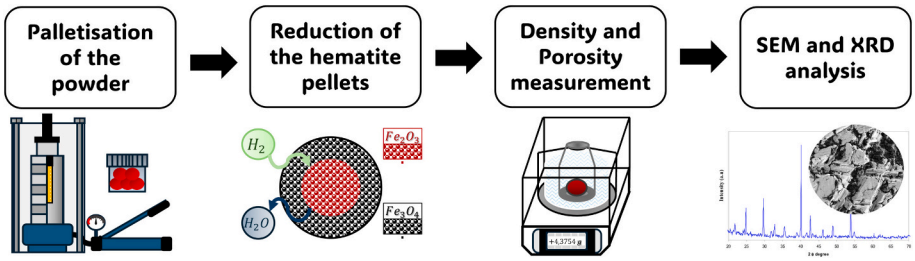

Fig. 2. Step-by-step graphical representation of the experimental procedure for porosity determination.

through a combined analysis of SEM images using ImageJ software and supported by phase identification through XRD. This phase-specific porosity information was then implemented in the kinetic model to better represent the evolving resistance to hydrogen diffusion across the various stages of the reduction process. The reduction experiments were carried out under H_2/Ar in order to isolate the microstructural evolution associated with the hydrogen-driven reduction pathway. In the A-DRI model, the porosity-metallisation relationships obtained from these experiments are applied to the H_2-driven iron oxide reduction step, since ammonia is treated as a hydrogen carrier and not as the direct reducing species. Therefore, the experimentally derived parameters describe the structural evolution associated with oxygen removal, phase transformation, pore growth, and densification during hydrogen reduction. In this sense, the porosity data are used primarily as a function of metallisation degree, rather than as time-dependent kinetic curves specific to the H_2/Ar atmosphere.

This transferability assumption introduces uncertainty, as the actual A-DRI atmosphere contains N_2 and may include residual NH_3. Differences in gas composition may affect external mass transfer and effective diffusivity, while residual NH_3 may promote transient nitridation under favourable temperature and composition conditions [32,33,35]. These effects are not explicitly resolved in the present experimental campaign and should be addressed in future NH_3- or H_2/ N_2-based pellet reduction experiments.

Further details on the experimental apparatus, gas delivery system, and porosity measurement procedures are provided in Supplementary Section S1.

2.3. Kinetic shaft-furnace model (PFR-USC framework)

The objective of the mathematical model is to describe the thermochemical behaviour of the counter-current shaft furnace, where hematite pellets descend from the top while a hot reducing gas mixture (H_2, N_2, and NH_3) is injected from the bottom. The model combines a Plug Flow Reactor (PFR) formulation at the reactor scale with an Unreacted Shrinking Core (USC) kinetic model to describe the reduction of individual pellets. In the present work, the USC framework is implemented in a multi-interface form, where the moving boundaries between hematite, magnetite, wüstite, and metallic iron are tracked explicitly, allowing multiple solid phases to coexist within the same pellet at intermediate metallisation degrees. This multiscale approach captures both axial variations of gas composition and temperature, and the local reduction rate of the pellets along the furnace height. Table 2 provides a structured summary of the key assumptions underlying the thermodynamic and kinetic formulation of the shaft furnace model. Among the assumptions listed in the table, a key point is that iron oxide reduction is treated as hydrogen-driven, while ammonia decomposition is modelled separately as a finite-rate catalytic reaction occurring on metallic iron surfaces in the lower high-temperature region of the furnace. Therefore, NH_3 conversion is not imposed a priori in the kinetic model, but is calculated locally as a function of temperature, gas composition, available metallic iron surface, and approach to thermodynamic equilibrium. Under this framework, the reduction kinetics remain governed by H_2, while ammonia acts as a hydrogen carrier through in-situ catalytic cracking. The full formulation of the ammonia-cracking sub-model is reported in Supplementary Section. Consequently, the experimentally derived porosity-metallisation relationships are applied to the H_2-driven reduction step of the A-DRI model, while possible gas-composition effects are treated as model uncertainties.

To simplify the coupling between ammonia decomposition and iron oxide reduction, the shaft furnace is discretized into two idealized control volumes. The model is initialized at the top of the shaft furnace,

Table 2
Summary of the main modelling assumptions.

Category	Main assumptions
Furnace flow configuration (PFR)	The shaft furnace is modelled as a counter-current Plug Flow Reactor. Radial dispersion is neglected. Gas and solids are treated as homogeneous phases within each control volume. Pellets are assumed spherical and monodisperse.
Reaction treatment	Iron oxide reduction occurs via H_2. Ammonia is not treated as a direct reducing agent in the kinetic model; instead, its decomposition is described through a finite-rate catalytic cracking model, and the generated H_2 contributes to the reducing gas mixture.
Ammonia decomposition	NH_3 decomposition is activated in the lower high-temperature region of the furnace, where the solid phase is predominantly metallic iron. The reaction is modelled as a heterogeneous catalytic process with finite-rate kinetics and equilibrium correction [31], as detailed in Supplementary Section.
Kinetic model (USC)	The reduction kinetics follow the Unreacted Shrinking Core model. The overall reaction rate is controlled by three resistances: gas phase transport, diffusion in porous media, and surface chemical kinetics. The kinetics are treated as zero-order with respect to the gaseous species.
Local thermodynamics and heat transfer	Gas and solid within each control volume are assumed to reach local thermal equilibrium. For numerical stability, temperature evolution is solved in a co-current formulation, even though mass balances are counter-current. Gas-solid heat exchange is modelled using an average convective heat transfer coefficient, and reaction enthalpies contribute to the energy balance.
Macroscopic modelling approach	Axial profiles of temperature, flow rates, and species composition are obtained from discrete mass and energy balances applied to each control volume. Boundary conditions for both gas and solid streams are taken from the thermodynamic model. Mechanical effects such as pellet fracture, decrepitation, or swelling-induced breakage are not included. The porosity–metallisation relationships measured under H_2/Ar are used as structural descriptors for the H_2-driven reduction step. Pellet structural evolution is assumed to be primarily governed by metallisation degree, while possible N_2 effects on gas transport and effective diffusivity are treated as model uncertainties.

where fresh hematite pellets enter. In the first control volume, only hydrogen-based reduction reactions are considered and allowed to proceed until full metallisation is achieved. In the second control volume, ammonia decomposition is activated and described through a finite-rate heterogeneous catalytic model on metallic iron surfaces. The local cracking rate is calculated at each axial node by accounting for reaction kinetics, gas composition, metallic iron availability, and the approach to thermodynamic equilibrium, as detailed in Supplementary Section.

The axial separation between the reduction and ammonia-cracking domains represents a one-dimensional approximation of the shaft furnace. In real reactors, partial spatial overlap between iron oxide reduction and NH_3 decomposition may occur due to local gradients in temperature, gas composition, residence time, and metallisation degree. This overlap may be further promoted by the autocatalytic effect of porous metallic iron on NH_3 decomposition, as reported by Ma et al. [23]. This limitation is considered when discussing the kinetic model results.

The molar flow rate of each gaseous and solid species is updated along the height of the shaft furnace through discrete species balances applied to each control volume of the PFR model. In compact form, the species balance for component j is written as:

$$\dot{n}_j(z+dz) = \dot{n}_j(z) \pm A_p \cdot \nu_j \cdot R_j \tag{3}$$

where $\dot{n}_j(z)$ and $\dot{n}_j(z+dz)$, in mol/s, are the inlet and outlet molar flow rates, respectively; ν_j is the stoichiometric coefficient (positive for products, negative for reactants); A_p is the total pellet surface area within the control volume in m^2; and R_i [mol/m^2/s] is the rate of formation or consumption per unit surface.

Full species-balance expressions for H_2, H_2O, N_2, and NH_3, and the iron-oxide phases are reported in the Supplementary Material.

Although the shaft furnace is physically a counter-current system, with ascending gases and descending solids, only the mass balances are solved in a counter-current formulation. For the thermal part of the model, a co-current approximation is adopted: gas and solid temperatures are advanced along the axial coordinate in the same direction. This numerical strategy avoids the iterative coupling that would otherwise be required to match gas-solid heat exchange between two oppositely flowing streams. In each control volume, the temperature evolution of the gas and solid phases is governed by two contributions:

(i) convective heat exchange between the bulk gas and the external surface of the pellets, and
(ii) endothermic heat absorbed by chemical reactions, namely the hydrogen-based reduction of iron oxides and, once activated, the thermal decomposition of ammonia.

Both effects act simultaneously on the pellet external surface area A_{sp}, defined as the total wetted surface of the pellets contained in the control volume. Assuming a constant surface heat flux q_s'' [W/m^2], the temperature update for gas and solid reads:

$$T_{gas}(i+1) = T_{gas}(i) + \frac{q''_{s,gas} \cdot A_{sp}}{\dot{n}_{gas} \cdot \tilde{c}_{p,gas}} \tag{4}$$

$$T_{sol}(i+1) = T_{sol}(i) + \frac{q''_{s,sol} \cdot A_{sp}}{\dot{n}_{sol} \cdot \tilde{c}_{p,sol}} \tag{5}$$

with the surface heat fluxes defined as:

$$q''_{s,gas} = h_{conv} \cdot \left(T_g(i) - T_s(i)\right) + \sum_{i=1}^{3} \Delta_r H_i^{\circ}\left(T_{sol}(i)\right) \cdot R_i(i) \cdot f_{gas} \tag{6}$$

$$q''_{s,sol} = h_{conv} \cdot \left(T_g(i) - T_s(i)\right) + \sum_{i=1}^{3} \Delta_r H_i^{\circ}\left(T_{sol}(i)\right) \cdot R_i(i) \cdot f_{sol} \tag{7}$$

where f_{gas} and f_{sol} are dimensionless factors used to allocate the share of endothermic heat between gas and solid, h_{conv} is the overall heat transfer coefficient in $W/m^2/K$, $\Delta_r H_i$ is the enthalpy change of each intermediate reduction reaction in J/mol evaluated at the solid temperature, as it is assumed that the solid-gas reaction occurs within the pellet, and R_i is the reaction rate of the reduction reactions in $mol/m^2/s$.

The iron oxide reduction kinetics are modelled using the USC model, which assumes that the reaction occurs at a sharp interface separating the reacted outer layer from the unreacted core. Initially, iron ore particles are considered fully composed by hematite. As reduction proceeds, a metallic iron layer forms increasing the diffusion resistance, and the unreacted core progressively shrinks until it is completely reduced [34].

The overall reaction rate of an individual ore particle is governed by the cumulative resistances arising from the following key mechanisms:

(i) gas phase transport resistance, involving the mass transport of the gaseous reactant from the bulk flow to the ore surface, and counter-diffusion of products;
(ii) diffusion in porous media resistance, which entails the diffusion of the gaseous reactants through the porous reduced solid layer;
(iii) surface chemical kinetics resistance, associated with the rates of chemical reaction between the metal oxide and the gaseous reactant.

Kinetic equations of hydrogen reduction reaction of iron ore are based on USC model for spherical particles, according to the model proposed by Levenspiel [35] (Eq. (8)):

$$\begin{cases} R_{Fe_2O_3} = \left(\dfrac{1}{k_{gas}} + \sum_{i=1}^{3} R \cdot \dfrac{R-r}{r \cdot D_{eff}} + \dfrac{R_p^2}{r^2 \cdot k''_{Fe_2O_3}}\right)^{-1} \\ R_{Fe_3O_4} = \left(\dfrac{1}{k_{gas}} + \sum_{i=1}^{2} R \cdot \dfrac{R-r}{r \cdot D_{eff}} + \dfrac{R_p^2}{r^2 \cdot k''_{Fe_3O_4}}\right)^{-1} \\ R_{FeO} = \left(\dfrac{1}{k_{gas}} + r_{Fe} \cdot \dfrac{r_{Fe} - r_{FeO}}{r_{FeO} \cdot D_{eff,Fe}} + \dfrac{R_p^2}{r^2 \cdot k''_{FeO}}\right)^{-1} \end{cases} \tag{8}$$

where:

- k_{gas} describes the gas-solid mass-transfer coefficient;
- D_{eff} is the effective diffusivity through the porous layer;
- k'' represents the intrinsic surface reaction constant.

A detailed description of the kinetic parameters, diffusivities, temperature dependencies, and physical meaning of each term is provided in the Supplementary Material.

In order to quantify the relative contribution of surface chemical kinetics and intra-particle mass transport to the overall reduction rate, a dimensionless parameter analogous to the Thiele modulus was evaluated. Within the USC model framework, this parameter corresponds to a Damköhler-type number, defined as the ratio between the characteristic surface reaction rate and the rate of diffusion through the porous reduced iron layer [36]:

$$\phi = \frac{R_p \cdot k_s}{D_{eff}} \tag{9}$$

where R_p is the pellet radius, k_s the intrinsic surface reaction rate constant, and D_{eff} the effective diffusivity through the porous reduced iron layer. Values of ϕ provide an indication of the dominant resistance controlling the reduction process, distinguishing between diffusion-controlled and reaction-controlled regimes.

The USC model enables tracking the evolution of the internal structure of iron oxide pellets along the furnace height by explicitly accounting for the growth and shrinkage of the concentric layers

associated with each solid phase (hematite, magnetite, wüstite, and metallic iron).

Reduction proceeds sequentially from the pellet surface toward the core, and the progression of each reduction step is represented by the inward movement of the corresponding reaction front.

The evolution of the radius of each solid phase is calculated by enforcing mass conservation at the pellet scale. For each reduction step, the decrease in the volume of a given phase is proportional to the reaction rate predicted by the USC kinetic model (Eqs. (10–13)).

$$r_{Fe_2O_3}(i+1) = \left\{ r^3_{Fe_2O_3}(i) - \left[{}^{3}/_{4\pi} \cdot \tilde{\rho}_{Fe_2O_3} \cdot (3 \cdot S_{pel} \cdot R_{Fe_2O_3}) \right] \right\}^{\frac{1}{3}} \tag{10}$$

$$r_{Fe_3O_4}(i+1) = \left\{ r^3_{Fe_3O_4}(i) - \left[{}^{3}/_{4\pi} \cdot \tilde{\rho}_{Fe_3O_4} \cdot (3 \cdot S_{pel} \cdot R_{Fe_3O_4}) \right] \right\}^{\frac{1}{3}} \tag{11}$$

$$r_{FeO}(i+1) = \left\{ r^3_{FeO}(i) - \left[{}^{3}/_{4\pi} \cdot \tilde{\rho}_{FeO} \cdot (3 \cdot S_{pel} \cdot R_{FeO}) \right] \right\}^{\frac{1}{3}} \tag{12}$$

$$r_{Fe}(i+1) = \left\{ r^3_{Fe}(i) - \left[{}^{3}/_{4\pi} \cdot \tilde{\rho}_{Fe} \cdot (3 \cdot S_{pel} \cdot R_{Fe}) \right] \right\}^{\frac{1}{3}} \tag{13}$$

This formulation directly links the pellet-scale kinetics to the internal phase distribution and provides the geometric basis for the radial phase profiles discussed in the Results section.

3. Results

Section 3 presents and discusses the main results of this work. Section 3.1 reports the experimental findings on porosity evolution, phase distribution, and microstructural changes during hydrogen reduction. Section 3.2 analyses the outcomes of the thermodynamic model, while Section 3.3 examines the kinetic shaft-furnace simulations, highlighting the implications of ammonia-based operation on temperature profiles, reaction rates, and metallisation behaviour.

3.1. Experimental characterisation of porosity and phase evolution

The experimental data used to analyse the evolution of metallisation, porosity and swelling during hydrogen reduction are summarised in Table 3. These measurements form the basis for constructing correlations between global porosity and metallisation, which are later implemented in the kinetic model.

These results allow to establish a correlation between the degree of metallisation and the reduction time, the overall porosity, and the Reduction Swelling Index (RSI), as illustrated in Fig. 3. The metallisation curve (Fig. 3a) exhibits a non-linear dependence on reduction time, consistent with previous studies [34,37,38]; full metallisation (about 100%) is achieved after 180 min.

The skeletal volume decreases almost linearly with increasing metallisation (Fig. 3b). This behaviour reflects the progressive conversion of

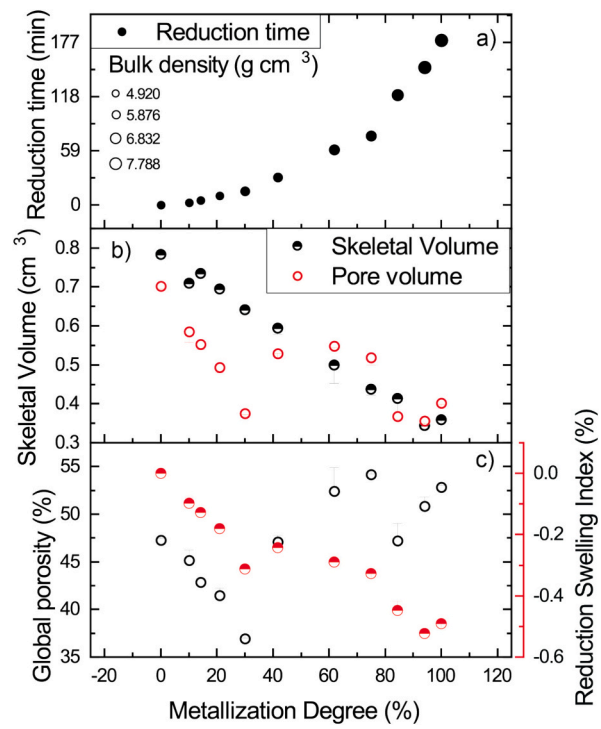

Fig. 3. a) Metallisation degree of iron pellets as a function of reduction time; b) Evolution of pore and skeletal volumes as functions of metallisation degree; c) Global porosity and Reduction Swelling Index (RSI) as functions of metallisation degree.

hematite → magnetite → wüstite → metallic iron, whose densities increase from 5.1 to 7.86 g/cm^3. Consequently, the global porosity trend is governed by the evolution of pore volume relative to the shrinking skeletal volume.

The RSI behaviour (Fig. 3c) measured ex-situ differs partially from the in-situ observations in [21], that inherently include the contribution of thermal expansion at the reduction temperature. Here, volumetric quantities are measured at room temperature, isolating the microstructural contribution to swelling. The RSI decreases initially up to about 30% metallisation, then reaches a maximum around 40%, before decreasing again at higher metallisation levels. Both this work and [21] exhibit the same distinct swelling peak, corresponding to the regime where wüstite formation is maximized relative to metallic iron [22]. Wüstite typically exhibits a more porous and voluminous morphology, which promotes swelling; once metallic iron forms, densification and recrystallisation reduce pore volume and thus decrease swelling.

Fig. 4 shows cross-sectional views of four reduced pellets (a) 10 min, b) 1 h, c) 5 min, and d) 3 h, subsequently embedded in epoxy resin. These images reveal the progressive inward movement of the reduction front and highlight the development of distinct radial zones (edge,

Table 3
Experimental mass measurements used to calculate the porosity of reduced pellets.

Parameters	Reduction Time [min]										
	0	2.5	5	10	15	30	60	75	120	150	180
Initial Mass [g]	3.86	3.66	3.83	3.80	3.84	3.86	3.75	3.68	3.81	3.74	3.87
Mass of the reduced samples [g]	3.86	3.55	3.67	3.56	3.49	3.38	3.05	2.85	2.84	2.68	2.69
Metallisation Degree [%]	0%	10%	14%	21%	30%	42%	62%	75%	84%	94%	100%
Pores Volume [cm^3]	0.70	0.59	0.55	0.49	0.38	0.53	0.55	0.52	0.37	0.36	0.40
Skeletal Volume [cm^3]	0.79	0.71	0.74	0.70	0.64	0.59	0.50	0.44	0.41	0.34	0.36
Bulk Density [g/cm^3]	4.91	5.00	4.99	5.13	5.45	5.69	6.13	6.51	6.90	7.79	7.50
Global Porosity [%]	47.2%	45.2%	42.9%	41.5%	37.0%	47.1%	52.4%	54.2%	47.2%	50.8%	52.8%
RSI [%]	0.0%	−8.4%	−13.0%	−19.1%	−31.5%	−24.8%	−27.7%	−32.8%	−46.9%	−51.5%	−49.1%
Porosity Variation [%]	0.0%	−4.4%	−9.2%	−12.1%	−21.7%	−0.2%	10.9%	14.8%	0.0%	7.6%	11.9%

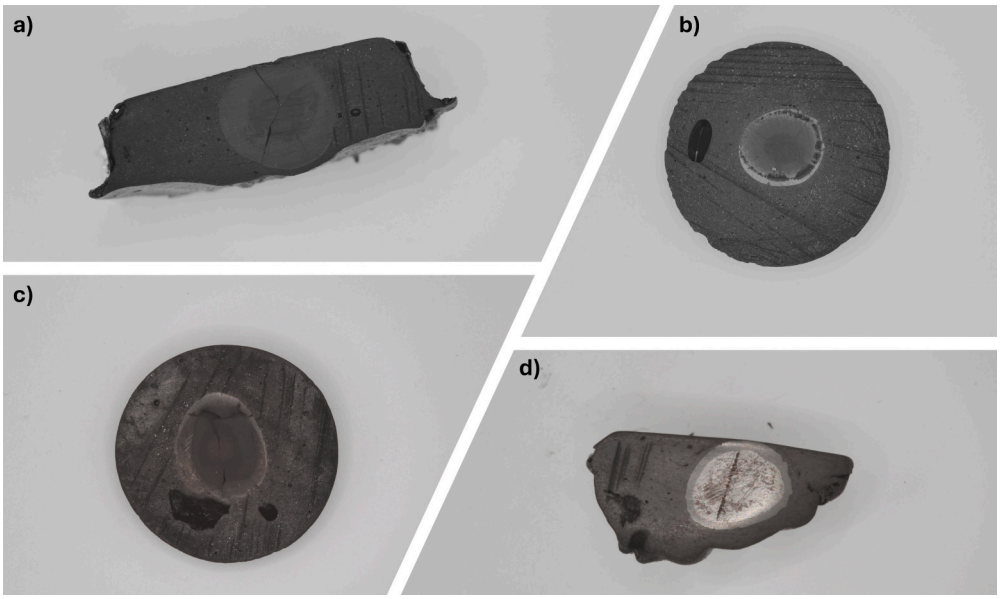

Fig. 4. Cross-sectional views of reduced pellets embedded in epoxy resin after (a) 5 min, (b) 10 min, (c) 1 h, and (d) 3 h of reduction.

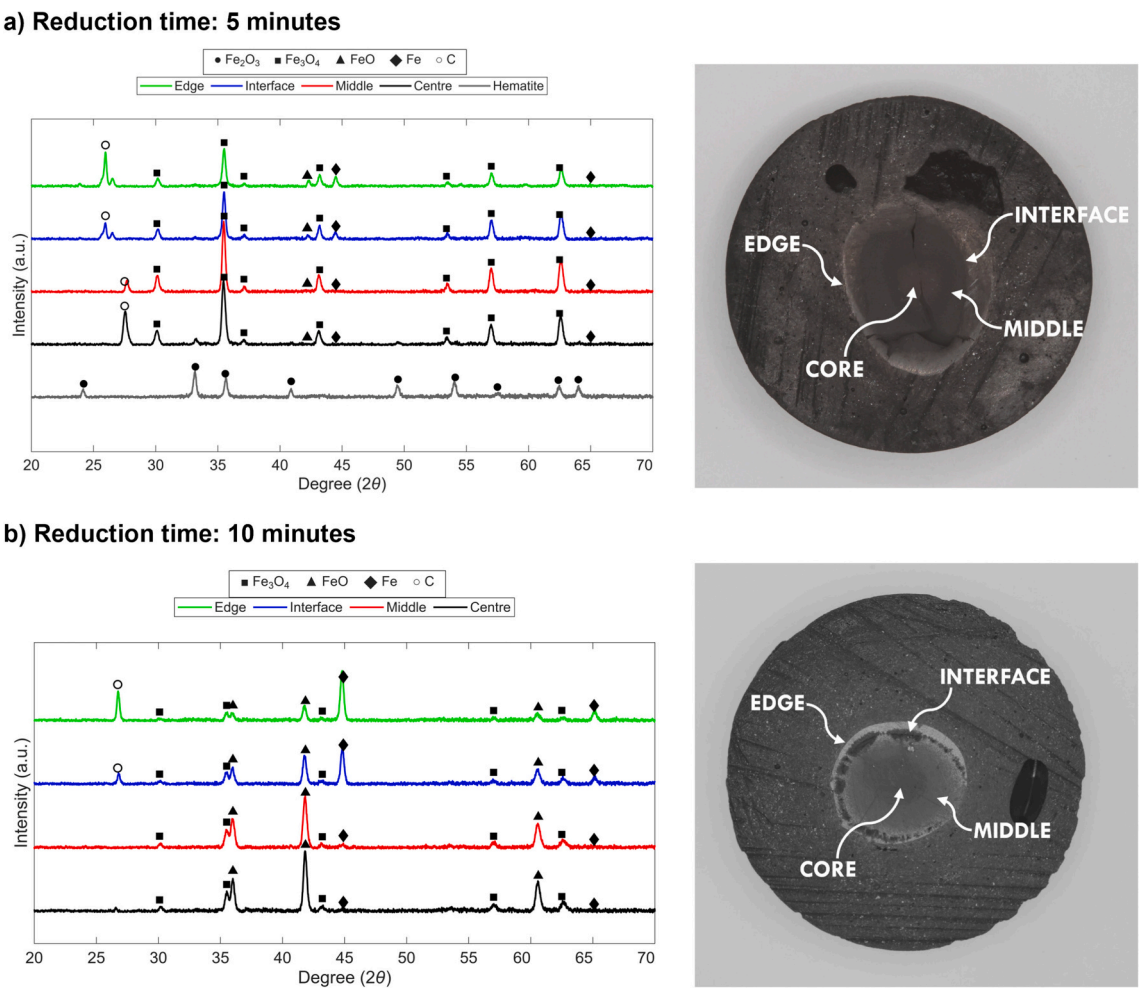

Fig. 5. XRD intensity vs. 2θ for a pellet reduced for 5 min (a) and for 1 h (b), measured at four radial positions (centre, middle, interface, edge). The image on the right marks the sampling locations.

interface, middle, core).

Fig. 5 shows the XRD phase distribution at multiple radial positions for pellets reduced for 5 min and 1 h. In the pellet reduced for 5 min (Fig. 5a), with a metallisation degree of 14% and an overall porosity of 43%, the core predominantly exhibits magnetite along with residual hematite. At the middle position, hematite peaks disappear, leaving only

magnetite. Moving from the interface to the edge, peaks of wüstite and metallic iron progressively emerge and intensify, while magnetite signals diminish. A carbon peak, attributed to the epoxy resin, is also detected only at the interface and edge, indicating incomplete degassing during resin curing.

In the pellet reduced for 1 h (Fig. 5b), metallisation degree of 60% and an overall porosity of 50%, a completely different composition is found. Magnetite is still present at all four radial positions, although with low intensity and fading toward the edge (notably around 57°). At the centre and middle positions, wüstite predominates, while at the interface and edge, metallic iron becomes the dominant phase. At a metallisation degree of 60%, wüstite, magnetite, and metallic iron coexist throughout the pellet.

Consistently with the findings reported in [39], the reduction of hematite by hydrogen proceeds in a stepwise manner. Wüstite formation is observed only after the complete consumption of hematite, indicating that the hematite-to-magnetite reduction step is completed before the onset of the magnetite-to-wüstite transformation. In contrast, the appearance of metallic iron is not strictly confined to the complete disappearance of magnetite, and partial coexistence of magnetite, wüstite, and metallic iron is observed during advanced stages of reduction.

Based on this experimental evidence, the kinetic model adopts a semi-sequential reduction scheme, enforcing complete consumption of hematite prior to activating the magnetite-to-wüstite reaction, while allowing the wüstite-to-iron reduction to proceed concurrently with residual magnetite.

At higher magnifications, SEM images (Fig. 6a and Fig. 6b) clearly reveal the crystallographic and morphological differences between hematite and magnetite. Hematite displays a hexagonal crystal structure, typically forming tabular, rhombohedral, or plate-like grains. In contrast, magnetite exhibits an inverse spinel cubic structure with a more compact and dense morphology. Magnetite grains are generally observed in granular or massive forms and exhibit lower porosity compared to hematite. Notably, the grain size of magnetite is significantly larger than that of hematite. This observation suggests that the reduction from hematite to magnetite is accompanied by grain growth and an increase in grain volume. While hematite consists of smaller and more numerous grains, the transformation to magnetite results in fewer but larger grains. Under the investigated conditions (800 °C and short treatment time), thermal sintering is expected to be limited, as both hematite and magnetite exhibit low densification rates at this temperature [37]. Therefore, the observed grain enlargement can be primarily attributed to the reduction process rather than to significant sintering effects.

Fig. 6c, Fig. 6d and Fig. 6e show, at 3× magnification, the differences in porosity respectively for the 1 h reduced pellet the pellet in the "centre," "middle," and "core" areas at varying distances from the centre. The core remains the only region with minimal structural changes during the reduction process, irrespective of the type of iron oxide. Notably, the middle section appears more porous than the edge. This is likely due to the formation of metallic iron in the outer layer during reduction from wüstite. Wüstite is inherently more porous than magnetite and metallic iron, and as reduction progresses, the pellet becomes less porous when wüstite is converted into pure iron. The agglomeration characteristic of metallic iron further decreases porosity, slowing the diffusion of the reducing gas into the interior of the solid. Therefore, the reduction process is slower in regions where pure iron is formed, as the presence of iron and its porosity limits the diffusion rate of the reducing gas. The analysis of these three images using ImageJ yielded porosity values of 38%, 71%, and 62% for the centre, middle, and edge, respectively. This confirms that the production of pure iron leads to a decrease in porosity, while wüstite is associated with higher porosity levels.

Although the experiments were performed under H_2/Ar, the resulting porosity–metallisation correlations are used here as structural descriptors of the pellet at a given conversion state during the H_2-driven reduction pathway.

3.2. Thermodynamic modelling results

The coupled mass, molar and thermal effects resulting from ammonia cracking and iron-oxide reduction are summarised in Fig. 7, which integrates the flow diagrams and the corresponding energy balances for both the cooling and reducing zones.

In the cooling zone (Fig. 7a), ammonia injected at 25 °C absorbs

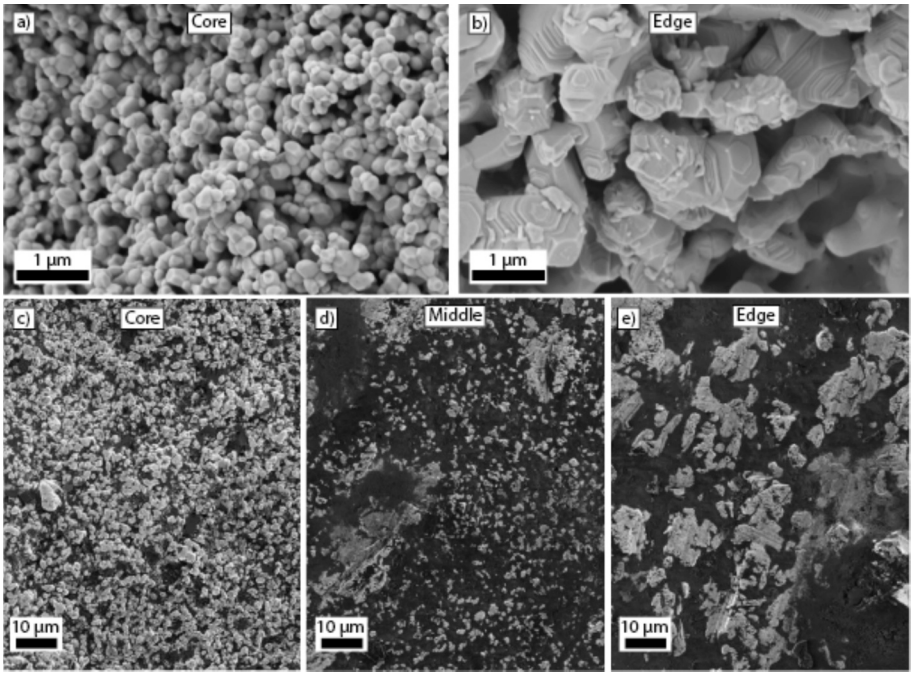

Fig. 6. SEM images of the 5 min a) b) and 1 h c) d) e) reduced pellet at 3× magnification, captured at three distances from the centre: Centre, Middle, and Edge, arranged from left to right, highlighting the morphological changes as the distance from the pellet core increases.

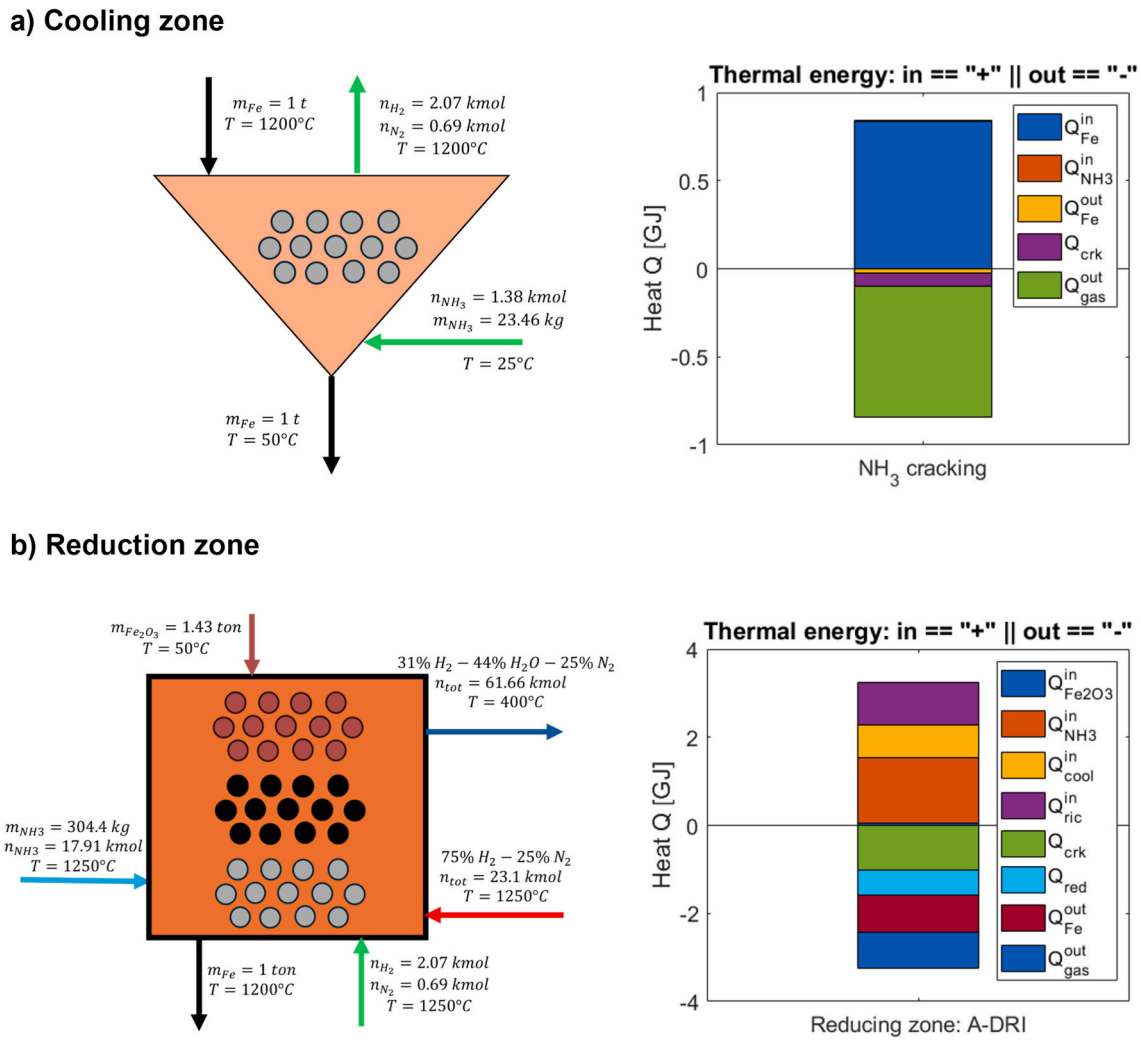

Fig. 7. Integrated thermodynamic representation of the A-DRI process. (a) Mass and molar flow diagram of the cooling zone and corresponding energy balance of the cooling zone. (b) Mass and molar flow diagram of the reducing zone and corresponding energy balance of the *reducing zone.* Heat flows can be entering (positive) or exiting (negative) from the zone.

sensible heat from the descending metallic iron and undergoes complete thermal cracking. The balance of sensible cooling of the solids, sensible heating of the gas, and the endothermic heat of cracking determines the maximum amount of NH_3 that can be decomposed while still delivering an outlet gas stream at 1200 °C. Under these conditions, 23.46 kg NH_3 per tonne of Fe are cracked, generating 2.07 kmol H_2 and 0.69 kmol N_2, which subsequently feed the reducing zone.

In the reducing zone (Fig. 7b), fresh ammonia, recirculated off-gas, and the cracked gas from the cooling zone mix at the bustle level. Their combined sensible heat, together with the endothermic demand of the reduction reactions, establishes the shaft-furnace thermal budget. The thermodynamic analysis shows that a recirculation fraction of 59% is required to provide the sensible heat needed to sustain both ammonia cracking and hydrogen-based reduction. The recirculated stream, composed of 31% H_2, 44% H_2O and 25% N_2, is reheated to 1250 °C before entering the furnace.

A parametric sensitivity analysis indicates that increasing the recirculation fraction raises the exhaust-gas temperature above the desired limit, whereas increasing the fresh-ammonia feed enriches the endothermic load and consequently lowers the exhaust temperature if recirculation is kept constant. These opposing effects quantify the thermal trade-offs that govern viable A-DRI operation and define the boundary conditions used in the kinetic model.

Table 4 summarizes the thermodynamic input required to initialise the kinetic shaft-furnace model. The stoichiometric hydrogen demand for complete hematite reduction is 26.86 kmol H_2 per tonne of iron, which corresponds to 304.39 kg of fresh ammonia. This value

Table 4
Thermodynamic outputs used as boundary conditions for the kinetic shaft-furnace model.

Parameter	Value	Unit
Ammonia cracked in cooling zone	23.46	kg NH_3 per t Fe
H_2 produced from cracked NH_3	2.07	kmol H_2 per t Fe
N_2 produced from cracked NH_3	0.69	kmol N_2 per t Fe
Ammonia-to-hematite mass ratio	21.3	kg NH_3 / kg Fe_2O_3
Hydrogen required for reduction	53.72	kg H_2 per t Fe
Hydrogen required (molar)	26.86	kmol H_2 per t Fe
Stoichiometric ammonia requirement	17.90	kmol NH_3 per t Fe
Recirculation gas composition	31% H_2–44% H_2O - 25% N_2	molar basis
Recirculation fraction	59%	% of outlet gas
Recirculated gas / fresh NH_3	1.30	kmol recirc. / kmol NH_3
Exhaust gas / fresh NH_3	3.44	kmol out / kmol NH_3

determines the ammonia injection rate in the reducing zone: the amount of NH_3 supplied is sized such that - after complete cracking - it provides exactly the hydrogen required to obtain 1 t of fully metallised pellets (100 wt% Fe) at the furnace outlet (reducing zone outlet). In addition, the H_2/N_2 stream generated in the cooling zone, the recirculated gas composition and flow rate, and the inlet temperature levels reported in Table 4 are transferred to the PFR-USC model as boundary conditions. The kinetic model then recalculates the local axial evolution of gas composition, temperature, reaction rates, and metallisation degree along the furnace height.

3.3. Kinetic shaft-furnace model results

Using the modelling framework introduced in Section 2.3, the kinetic simulations were initiated at the inlet of fresh hematite pellets and solved along the furnace height to obtain the coupled evolution of gas composition, temperature, reaction rates, and metallisation degree. Within the reduction domain, only hydrogen-based reduction reactions are active. The simulation proceeds until full metallisation is achieved, after which the ammonia-cracking domain is activated.

The temperature profile of the solid and gas is determined by the interplay between reaction heat and convective heat transfer. The initial temperature variation illustrated in Fig. 8a in the upper meters is primarily due to convective heat transfer and not to the hematite-to-magnetite reduction reaction that is characterized by a low exothermicity, resulting in a slower reaction rate due to the Arrhenius dependency on temperature. Once hematite is completely consumed in the solid phase, the more endothermic reactions, magnetite to wüstite and wüstite to pure iron, cause a further temperature rise, reaching approximately 1050 °C at the lowest height of the reducing zone control volume. This enthalpy release drives an increase in the temperature of both the gas and the solid phases, further accelerating the reaction process.

The reaction rate profile along the furnace height in Fig. 8b describes how the overall reaction kinetics change as the gas-solid mixture progresses down the furnace.

After rapid acceleration reaching a maximum, the reaction rate gradually decreases due to the shrinkage of the active unreacted core within the iron oxide particles and the increasing diffusion resistance through the porous product layer.

Once hematite is fully converted, the subsequent reduction steps proceed at rates governed by the local thermochemical conditions prevailing along the furnace height.

The rate of wüstite-to-metallic iron reduction tends to be higher than the preceding magnetite-to-wüstite reaction. However, as the magnetite-to-wüstite reaction produces three moles of wüstite per mole of magnetite, an excess of wüstite accumulates temporarily. This excess continues until the reaction rate of magnetite-to-wüstite slows significantly due to the near-complete consumption of magnetite.

The evolution of the metallisation degree along the furnace height, shown in Fig. 9a, provides valuable insights into the reduction kinetics in a DRI furnace. While laboratory experiments on hematite reduction typically report a significant slowdown during the final step, namely the conversion of wüstite to metallic iron, resulting in a progressively flatter metallisation curve, this behaviour is not observed under actual shaft-furnace operating conditions. In industrial reactors, the reducing gas is injected at the lower part of the furnace, where the temperature and hydrogen concentration are highest. These conditions accelerate the final and most critical reduction step, namely the conversion of wüstite to metallic iron, thereby sustaining a relatively rapid increase in metallisation degree near the furnace bottom.

Fig. 9b shows the axial evolution of the dimensionless Thiele modulus for the three successive reduction steps along the height of the shaft furnace. For all reactions, the Thiele modulus remains well below unity throughout the reactor height, indicating that the overall reduction kinetics are predominantly controlled by surface chemical reactions rather than by intra-particle mass transport limitations. A gradual increase of the Thiele modulus is observed moving upward along the furnace, reflecting the combined effects of temperature variation and the progressive evolution of pellet microstructure during reduction. Despite these variations, the consistently low values of the Thiele modulus suggest that diffusion through the product layer does not become rate-limiting under the investigated operating conditions, supporting the assumption of chemically controlled reduction kinetics across most of the furnace. Although diffusion through the product layer is not rate-limiting under the investigated conditions, it is still explicitly accounted for in the URC formulation to ensure consistency of the kinetic description over the full range of metallisation degrees.

Fig. 10a includes dashed vertical lines indicating selected metallisation degree values, for which stacked column charts report the corresponding molar fractions of the iron oxide phases (Fig. 10b). In addition, for metallisation degrees of 10%, 30%, and 60%, cross-sectional representations of the pellet are shown in Fig. 11, illustrating the radial distribution of the solid phases as derived from the Unreacted Shrinking Core model.

Consistent with the sequential reduction scheme adopted in the kinetic model and informed by experimental observations, the progressive depletion of magnetite beyond a metallisation degree of approximately 0.11 is accompanied by a simultaneous increase in the fractions of wüstite and metallic iron.

At a metallisation degree of 0.3, the molar fractions of magnetite, wüstite, and pure iron are 34%, 40%, and 26%, respectively.

In this condition, hydrogen can react with wüstite by diffusing into the pores of the metallic iron layer and with the magnetite in the even deeper layer by diffusing through the pores of the wüstite. It is evident

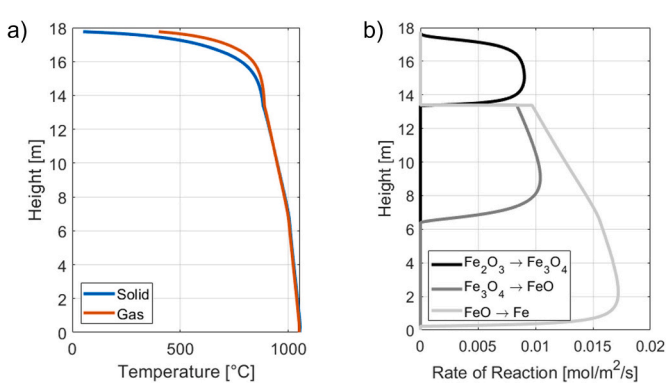

Fig. 8. (a) Temperature profile of the reducing gas mixture and iron ores along the shaft furnace height; (b) Reaction rate profile along the shaft furnace height for the three intermediate reduction steps.

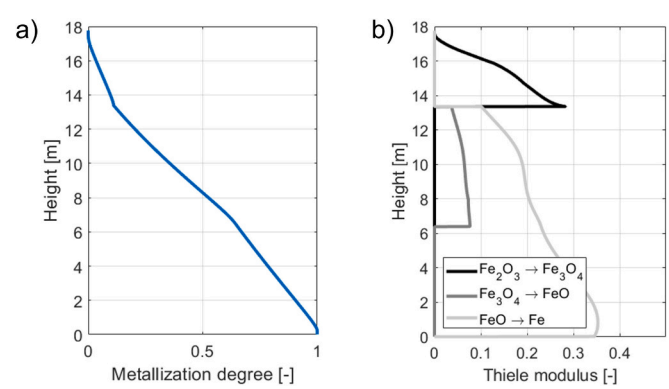

Fig. 9. a) Predicted evolution of the metallisation degree along the shaft furnace height. b) Axial evolution of the dimensionless Thiele (Damköhler-type) modulus calculated for the three reduction steps ($Fe_2O_3 \rightarrow Fe_3O_4$, $Fe_3O_4 \rightarrow FeO$, $FeO \rightarrow Fe$).

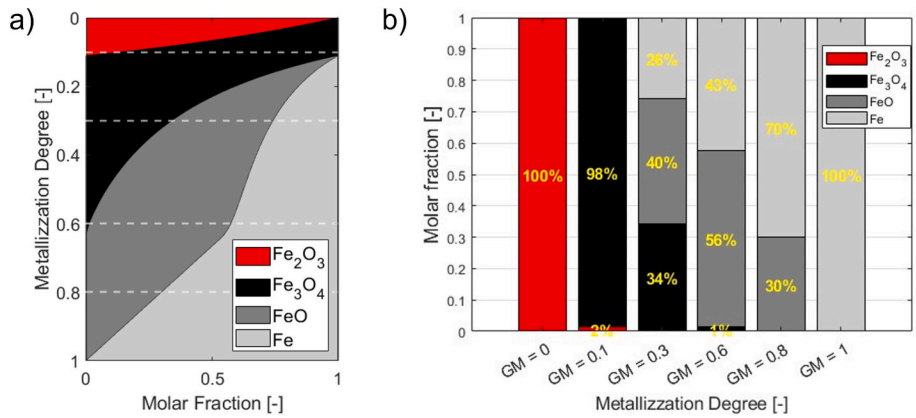

Fig. 10. (a) Evolution of the molar fraction of solid phases in relation to the metallisation degree of iron ores. (b) Molar fraction of each iron oxide phase (Fe_2O_3, Fe_3O_4, FeO) and pure iron (Fe) as a function of the metallisation degree (GM) of the iron ores.

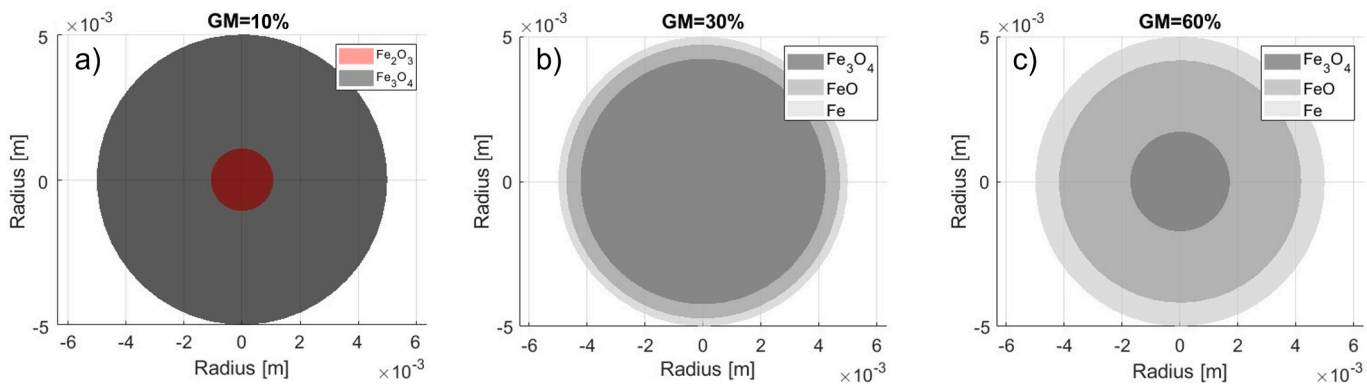

Fig. 11. Cross-sectional representation of an iron ore pellet at (a) 10% metallisation degree (GM = 10%); (b) 30% metallisation degree (GM = 30%); (c) at 60% metallisation degree (GM = 60%).

that to react with the magnetite to produce wüstite, hydrogen encounters an additional resistance compared to its reaction with wüstite alone.

Fig. 12a illustrates the molar composition of the reducing gas mixture at various points: at the exhaust exit, at the inlet of the first control volume, and at the bustle zone where fresh, hot ammonia mixes with the hot recirculated gas and gas from the cooling zone.

At the exhaust exit (top of the furnace), where the gas mixture exits after reacting, there is an increased concentration of the water vapour reaction product, reflecting a higher level of reduction completion in the lower sections of the furnace.

The reducing zone inlet represents an intermediate position where most of the iron oxide pellets have been reduced to pure iron, showing a high concentration of hydrogen and nitrogen with minimal ammonia left.

Finally, at the bustle zone fresh hot ammonia is injected and mixed with the recirculated reducing gas and the gas originating from the cooling zone; the gas mixture is characterized by a substantial ammonia fraction, together with hydrogen and nitrogen.

The ammonia decomposition reaction exhibits a significantly higher reaction rate compared to the hydrogen-based reduction of iron oxides. As a result, the conversion of hydrogen and nitrogen into ammonia occurs over a much shorter vertical section of the shaft furnace.

Fig. 12b shows the axial temperature profiles of both the gas and solid phases in the lower region of the shaft furnace, where the ammonia decomposition reaction is activated. Owing to its significantly higher reaction rate compared to the hydrogen-based reduction of iron oxides, ammonia decomposition occurs over a very limited vertical section of the furnace.

The high kinetic intensity of the cracking reaction results in a sharp local thermal effect, as the substantial endothermicity of ammonia decomposition rapidly absorbs sensible heat from both the gas and the solid. As evidenced by Fig. 12b, the kinetic model indicates that the temperature assumptions adopted in the preliminary thermodynamic analysis were somewhat optimistic. When ammonia injection is considered, the combined enthalpy demand of iron oxide reduction and ammonia cracking would require a reducing gas inlet temperature closer to 1400 °C to sustain the target operating conditions.

The requirement of reducing-gas inlet temperatures approaching 1400 °C represents a possible practical limitation of the reference A-DRI configuration. Such operating conditions may impose constraints

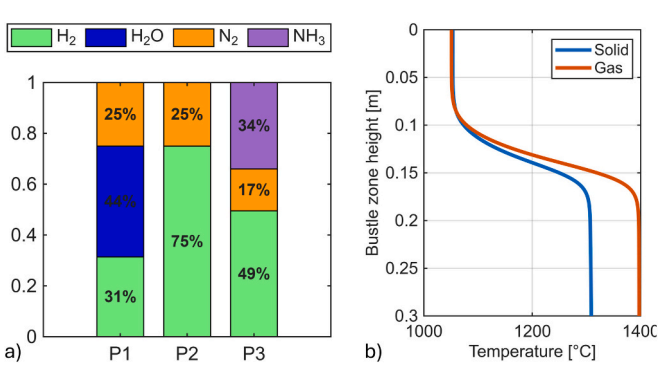

Fig. 12. (a) Molar fraction distribution of reducing gas species at selected locations within the shaft furnace: P1 denotes the exhaust gas exit, P2 the reducing zone inlet, and P3 the bustle height. (b) Temperature profiles of the DRI solid phase and reducing.

related to refractory material stability, heat losses, gas-heating energy demand, and possible pellet sticking, softening, or agglomeration. These aspects are not explicitly resolved in the present PFR-USC model and should be addressed in future process-scale assessments. The sensitivity case with increased recirculation partially mitigates this issue by lowering the required reducing-gas inlet temperature to slightly above 1300 °C, although at the expense of lower reaction rates and a longer reduction height.

The possible formation of iron nitrides is not explicitly included in the present model and represents an additional source of uncertainty. Literature data indicate that iron nitrides may form under NH_3-rich atmospheres at intermediate temperatures, but become unstable at higher temperatures. Mittal and Davis [40] reported Fe_4N decomposition over approximately 580–700 °C and observed little to no nitrogen incorporation in iron products reduced with NH_3 at 900–1000 °C. Therefore, persistent nitridation is expected to be limited in the high-temperature region considered here, although transient nitride formation in colder or NH_3-rich regions cannot be excluded.

For comparison, in the absence of ammonia injection, a reducing gas mixture composed of 75% H_2 and 25% N_2 typically reaches temperatures of approximately 1050 °C, which is consistent with the operating conditions expected for future commercial H-DRI plants.

To assess whether the required furnace height and temperature levels could be moderated, a sensitivity analysis was performed by increasing the recirculation gas flow rate by 10%. As expected, the higher recirculation rate leads to lower gas and solid temperatures at the bustle height, with the gas temperature decreasing to approximately 950 °C. Under these conditions, the required reducing gas injection temperature drops to just above 1300 °C, while the solid phase reaches around 1250 °C.

This reduction in temperature decreases the overall reaction rate, thereby extending the furnace height required to achieve complete reduction of hematite to metallic iron. However, the resulting operating window becomes more aligned with the temperature ranges typical of conventional H_2-based DRI processes.

4. Conclusions

This work combined experimental characterisation, thermodynamic analysis, and reactor-scale kinetic modelling to assess the feasibility of ammonia-based direct reduction of iron ores in a shaft furnace. By integrating experimentally derived microstructural parameters with a Plug Flow Reactor formulation and an Unreacted Shrinking Core kinetic model, the study provides a coupled thermal-kinetic assessment of how ammonia can be introduced into a DRI shaft furnace and how its in-situ cracking affects reduction performance.

The main conclusions can be summarised as follows:

- **Porosity evolution, swelling behaviour, and implications for kinetic modelling**

The combined evaluation of pellet skeletal volume and pore volume provides direct insight into the relationship between total swelling (RSI) and porosity evolution. The observed increase in porosity is primarily associated with the formation of wüstite, while the subsequent production of metallic iron leads to densification and partial pore closure, resulting in a reduction of porosity at high metallisation degrees. These trends, supported by SEM observations of phase-dependent microstructures, enabled the identification of phase-specific local porosity values. This information was essential for parameterising the USC kinetic model with realistic, phase-dependent transport properties, thereby strengthening the link between experimental observations and reactor-scale modelling.

- **Experimental validation of sequential reduction pathways**

Spatially resolved XRD analyses confirm that iron oxide reduction proceeds sequentially through the $Fe_2O_3 \rightarrow Fe_3O_4 \rightarrow FeO \rightarrow Fe$ pathway. Wüstite formation is observed only after the complete consumption of hematite, while partial coexistence of magnetite, wüstite, and metallic iron occurs at intermediate reduction stages. These observations directly informed the kinetic assumptions adopted in the USC model.

- **Thermodynamic constraints and recirculation requirements**

Preliminary thermodynamic analysis indicates that sustaining both hydrogen-based reduction and ammonia cracking requires significant sensible-heat input, which can be achieved through gas recirculation. A recirculation fraction of approximately 59% is required to satisfy the thermal demand while maintaining target operating temperatures.

- **Kinetic modelling of A-DRI integration**

The PFR-USC kinetic model captures the coupled effects of temperature, gas composition, diffusion limitations, and reaction kinetics along the shaft furnace height. While the thermodynamic model provides useful initial boundary conditions, the kinetic model reveals that ammonia decomposition introduces a strong, localized endothermic load, leading to higher required inlet gas temperatures and a modified temperature profile compared to H_2-DRI operation. Increasing the recirculation gas flow moderates peak temperatures but extends the furnace height required for complete metallisation.

Overall, the results suggest that A-DRI is feasible under the idealized thermodynamic and kinetic assumptions adopted in this work. However, practical implementation will require further validation of high-temperature operation, heat integration, pellet sticking and agglomeration behaviour, refractory constraints, and possible transient nitridation under representative NH_3-containing atmospheres.

Looking ahead, future work should validate the H_2/Ar-derived porosity and transport parameters under representative NH_3 and H_2/N_2 atmospheres, while also assessing balance-of-plant implications, including ammonia production costs, electrolyser energy demand, exhaust-gas hydrogen recovery, and heat-integration strategies. These analyses are required to quantify the economic competitiveness of A-DRI relative to H_2-DRI. Nevertheless, by reducing dependence on large-scale on-site hydrogen storage and distribution infrastructure, A-DRI represents an evolutionary and practical pathway toward large-scale decarbonisation of primary ironmaking.

Acronyms

A-DRI	Ammonia-based Direct Reduced Iron
BF	Blast Furnace
BOF	Basic Oxygen Furnace
DAQ	Data Acquisition System
DRI	Direct Reduced Iron
EAF	Electric Arc Furnace
H_2-DRI	Hydrogen-based Direct Reduced Iron
MFC	Mass Flow Controller
RES	Renewable Energy Sources
RSI	Reduction Swelling Index
SEM	Scanning Electron Microscopy
SCCM	Standard Cubic Centimeters per Minute
SF	Shaft Furnace
TPR	Temperature-Programmed Reduction
XRD	X-ray Diffraction
USC	Unreacted Shrinking Core

CRediT authorship contribution statement

Angelo Paziente: Writing – original draft, Visualization, Software, Methodology, Investigation, Formal analysis, Data curation. **Alessandro Magnino:** Writing – review & editing, Visualization, Validation, Supervision, Investigation. **Marta Gandiglio:** Writing – review & editing, Visualization, Supervision, Resources, Project administration, Investigation. **Luca Mastropasqua:** Writing – review & editing, Validation, Supervision, Resources, Project administration, Investigation, Funding acquisition, Data curation, Conceptualization.

Declaration of competing interest

The authors declare that they have no known competing financial interests or personal relationships that could have appeared to influence the work reported in this paper.

Acknowledgments

The authors gratefully acknowledge the funding from the Department of Mechanical Engineering and the College of Engineering to support the experimental activities of Angelo Paziente during his research stay at the Hydrogen and Electrochemical Research for Decarbonization (HERD) Laboratory at the University of Wisconsin-Madison in 2025. The authors also thank Eric Hintz and Zilong Zhuang for their support during sample preparation, and Shardul Singh and Zilong Zhuang for their contribution to the data analysis.

Appendix A. Supplementary data

Supplementary data to this article can be found online at https://doi.org/10.1016/j.cej.2026.178542.

Data availability

Data will be made available on request.

References

[1] World Steel Association, "2024 World Steel in Figures,", 2024. Accessed: Nov. 05, 2024. [Online]. Available: https://worldsteel.org/wp-content/uploads/World-Steel-in-Figures-2024.pdf.
[2] J. Somers, Technologies to decarbonise the EU steel industry Publications Office of the European Union, Luxembourg (2021), https://doi.org/10.2760/069150.
[3] World Economic Forum, Steel industry net-zero tracker, 2024. https://reports.weforum.org/docs/WEF_Net_Zero_Industry_Tracker_2024_Steel.pdf.
[4] Z. Fan, S.J. Friedmann, Low-carbon production of iron and steel: Technology options, economic assessment, and policy, Apr. 21, Cell Press. (2021), https://doi.org/10.1016/j.joule.2021.02.018.
[5] T. Watari, S. Hata, K. Nakajima, K. Nansai, Limited quantity and quality of steel supply in a zero-emission future, Nat. Sustainability 6 (3) (2023) 336–343, https://doi.org/10.1038/s41893-022-01025-0.
[6] Working Group III, *contribution to the Sixth Assessment Report of the Intergovernmental Panel on Climate Change Mitigation of Climate Change*, 2022 [Online]. Available: https://www.ipcc.ch/report/ar6/wg3/.
[7] L. Yang, et al., A review on production and application of direct reduced iron in gas-based shaft furnace–electric arc furnace route, J. Iron Steel Res. Int. 32 (3) (2025) 485–518, https://doi.org/10.1007/s42243-024-01377-1.
[8] IEA, Iron and Steel Technology Roadmap, Paris. Accessed: Nov. 05, 2024. [Online]. Available: https://www.iea.org/reports/iron-and-steel-technology-roadmap, 2020.
[9] IEA, Global Hydrogen Review 2023 (2023). https://www.iea.org/reports/global-hydrogen-review-2023.
[10] M. Shahabuddin, G. Brooks, M.A. Rhamdhani, Decarbonisation and hydrogen integration of steel industries: recent development, challenges and technoeconomic analysis, J. Clean. Prod. 395 (2023) 136391, https://doi.org/10.1016/j.jclepro.2023.136391.
[11] J. Cui, M. Aziz, Techno-economic analysis of hydrogen transportation infrastructure using ammonia and methanol, Int. J. Hydrog. Energy 48 (42) (2023) 15737–15747, https://doi.org/10.1016/j.ijhydene.2023.01.096.
[12] I. Energy Agency, Ammonia Technology Roadmap: Towards more sustainable nitrogen fertiliser production, 2021 [Online]. Available: https://www.iea.org/reports/ammonia-technology-roadmap.
[13] B. Sadeghi, P. Cavaliere, M. Bayat, N. Ebrahimzadeh Esfahani, A. Laska, D. Koszelow, Experimental study and numerical simulation on porosity dependent direct reducibility of high-grade iron oxide pellets in hydrogen, Int. J. Hydrog. Energy 69 (2024) 586–607, https://doi.org/10.1016/j.ijhydene.2024.05.050.
[14] P. Cavaliere, L. Dijon, A. Laska, and D. Koszelow, "Hydrogen direct reduction and reoxidation behaviour of high-grade pellets," Int. J. Hydrog. Energy, vol. 49 (2024), pp. 1235–1254, 2023, doi:https://doi.org/10.1016/j.ijhydene.2023.08.254.
[15] H. Kang, et al., Influence of hydrogen flow rate on multistep kinetics of hematite reduction, Int. J. Hydrog. Energy 49 (2024) 1255–1268, https://doi.org/10.1016/j.ijhydene.2023.08.295.
[16] M. Takeda, T. Onishi, S. Nakakubo, S. Fujimoto, Physical properties of iron-oxide scales on Si-containing steels at high temperature, Mater. Trans. 50 (9) (2009) 2242–2246, https://doi.org/10.2320/matertrans.M2009097.
[17] T.K. Sandeep Kumar, Investigation of sintering kinetics of magnetite pellets during induration, Licentiate thesis, Luleå University of Technology, Luleå, Sweden, 2015. ISBN 978-91-7583-406-1.
[18] A.A. Barde, J.F. Klausner, R. Mei, Solid state reaction kinetics of iron oxide reduction using hydrogen as a reducing agent, Int. J. Hydrogen Energy 41 (24) (2016) 10103–10119, https://doi.org/10.1016/j.ijhydene.2015.12.129. ISSN 0360-3199.
[19] T. Triana, G.A. Brooks, M.A. Rhamdhani, M.I. Pownceby, Iron oxide direct reduction and Iron nitride formation using Ammonia: review and thermodynamic analysis, Journal of Sustainable Metallurgy 10 (3) (2024) 1428–1445, https://doi.org/10.1007/s40831-024-00860-z.
[20] J. He, K. Li, J. Zhang, A.N. Conejo, Reduction kinetics of compact hematite with hydrogen from 600 to 1050°C, Metals (Basel) 13 (3) (2023), https://doi.org/10.3390/met13030464.
[21] A.A. El-Geassy, M.I. Nasr, M.M. Hessien, Effect of reducing gas on the volume change during reduction of iron oxide compacts, ISIJ Int. 36 (6) (1996) 640–649, https://doi.org/10.2355/isijinternational.36.640.
[22] L. Yi, Z. Huang, T. Jiang, L. Wang, T. Qi, Swelling behavior of iron ore pellet reduced by H2-CO mixtures, Powder Technol. 269 (2015) 290–295, https://doi.org/10.1016/j.powtec.2014.09.018.
[23] Y. Ma, J.W. Bae, S.H. Kim, M. Jovičević-Klug, K. Li, D. Vogel, D. Ponge, M. Rohwerder, B. Gault, D. Raabe, Reducing iron oxide with ammonia: A sustainable path to green steel, Adv. Sci. 10 (16) (2023) 2300111, https://doi.org/10.1002/advs.202300111.
[24] P.K. Sarangi, et al., Sustainable hydrogen through decomposition of ammonia and its derivatives by thermochemical processes: a review, Polska Akademia Nauk. (2024), https://doi.org/10.31545/intagr/187984.
[25] D.G. Loffler, L.D. Schmidt, Kinetics of NH3 decomposition on iron at high temperatures, J. Catal. 44 (2) (1976) 244–258, https://doi.org/10.1016/0021-9517(76)90395-X.
[26] S. Mittal, L.M. Davis, Rapid, efficient reduction of iron oxide with ammonia, Cell Rep. Phys. Sci. 6 (5) (2025), https://doi.org/10.1016/j.xcrp.2025.102551.
[27] S. Hosokai, Y. Kasiwaya, K. Matsui, N. Okinaka, T. Akiyama, Ironmaking with ammonia at low temperature, Environ. Sci. Technol. 45 (2) (2010) 821–826, https://doi.org/10.1021/ES102910Q.
[28] A.S.M. Handbook, Steel heat treating fundamentals and processes, ASM International 4A (2013), https://doi.org/10.31399/ASM.HB.V04A.9781627081658.
[29] K. Kiełbasa, R. Pelka, W. Arabczyk, Studies of the kinetics of ammonia decomposition on promoted nanocrystalline iron using gas phases of different nitriding degree, J. Phys. Chem. A 114 (13) (2010) 4531–4534, https://doi.org/10.1021/jp9099286.
[30] M. Jovičević-Klug, Y. Ma, P. Jovičević-Klug, J.M. Prabhakar, M. Rohwerder, D. Raabe, Thermal kinetics and nitriding effect of ammonia-based direct reduction of iron oxides, ACS Sustainable Chem. Eng. 12 (26) (2023) 9882–9896, https://doi.org/10.1021/ACSSUSCHEMENG.4C02363.
[31] Naoto Yasuda, Yuuki Mochizuki, Naoto Tsubouchi, Tomohiro Akiyama, Reduction and nitriding behavior of hematite with ammonia, ISIJ Int. 55 (4) (2015) 736–741, https://doi.org/10.2355/isijinternational.55.736. Released on J-STAGE April 26, 2015, Online ISSN 1347-5460, Print ISSN 0915-1559.
[32] Y. Fei, X. Guan, S. Kuang, A. Yu, N. Yang, A review on the modeling and simulation of shaft furnace hydrogen metallurgy: a chemical engineering perspective, ACS Engineering Au 4 (2) (2024) 145–165, https://doi.org/10.1021/acsengineeringau.3c00033.
[33] M. Jovičević-Klug, Y. Ma, P. Jovičević-Klug, J.M. Prabhakar, M. Rohwerder, D. Raabe, Thermal kinetics and Nitriding effect of Ammonia-based direct reduction of Iron oxides, ACS Sustain. Chem. Eng. 12 (26) (2024) 9882–9896, https://doi.org/10.1021/ACSSUSCHEMENG.4C02363.
[34] D. G. Löffler and L. D. Schmidt, "Kinetics of NH3 decomposition on iron at high temperatures*1," J. Catal., vol. 44, no. 2, pp. 244–258, Aug. 1976, doi:https://doi.org/10.1016/0021-9517(76)90395-X.
[35] A. Hammam, et al., Studies on the reduction behavior of Iron oxide pellet fines with hydrogen gas: mechanism and kinetic analysis, Journal of Sustainable Metallurgy 9 (3) (2023) 1289–1302, https://doi.org/10.1007/s40831-023-00721-1.
[36] O. Levenspiel, Chemical Reaction Engineering, 3rd ed., John Wiley & Sons, 1999. https://books.google.com/books/about/Chemical_Reaction_Engineering.html?id=vw48EAAAQBAJ.
[37] T. Melchiori, P. Canu, Improving the quantitative description of reacting porous solids: critical analysis of the shrinking core model by comparison to the generalized grain model, Ind. Eng. Chem. Res. 53 (22) (2014) 8980–8995, https://doi.org/10.1021/ie403030g.

[38] A. Heidari, N. Niknahad, M. Iljana, T. Fabritius, A review on the kinetics of iron ore reduction by hydrogen, Dec. 01, Materials (2021), https://doi.org/10.3390/ma14247540.

[39] A.A. El-Geassy, M.I. Nasr, Influence of the original structure on the kinetics of hydrogen reduction of hematite compacts, Trans. Iron Steel Inst. Jpn. 28 (8) (1988) 650–658, https://doi.org/10.2355/ISIJINTERNATIONAL1966.28.650.

[40] D. Wagner, O. Devisme, F. Patisson, D. Ablitzer, D.A. Ablitzer, A laboratory study of the reduction of iron oxides by hydrogen, in: Sohn International Symposium, Aug. 2006. San Diego, United States. [Online]. Available: https://hal.science/hal-00265636v1.